mater.scichina.com link.springer.com

Published online 14 April 2022 | https://doi.org/10.1007/s40843-022-2025-x
Sci China Mater 2022, 65(10): 2826–2832

Mn-doped SiGe thin films grown by UHV/CVD with room-temperature ferromagnetism and high hole mobility

Limeng Shen[1,2], Xi Zhang[1,2], Jiaqi Wang[3], Jianyuan Wang[3], Cheng Li[3] and Gang Xiang[1,2*]

ABSTRACT **In this work, silicon-germanium (SiGe) thin films are epitaxially grown on Ge substrates by ultra-high vacuum chemical vapor deposition and then doped with Mn element by ion-implantation and subsequent rapid thermal annealing (RTA). The characterizations show that the epitaxial SiGe thin films are single-crystalline with uniform tensile strain and then become polycrystalline after the ion implantation and following RTA. The magnetization measurements indicate that the annealed thin films exhibit Mn concentration-dependent ferromagnetism up to 309 K and the X-ray magnetic circular dichroism characterizations reveal the spin and orbital magnetic moments from the substitutional Mn element. To minimize the influence of anomalous Hall effect, magneto-transport measurements at a high magnetic field up to 31 T at 300 K are performed to obtain the hole mobility, which reaches a record-high value of ~1230 cm^2 V^{-1} s^{-1}, owing to the crystalline quality and tensile strain-induced energy band modulation of the samples. The first demonstration of Mn-doped SiGe thin films with room-temperature ferromagnetism and high carrier mobility may pave the way for practical semiconductor spintronic applications.**

Keywords: diluted magnetic semiconductor, Mn-doped SiGe, ferromagnetism, hole mobility, UHV/CVD

INTRODUCTION

Since the discovery of ferromagnetic (Ga,Mn)As [1], various diluted magnetic semiconductors (DMSs) based on groups III-V [1–3], II-VI [4–6], I-II-V [7–9], and IV [10–18] semiconductors have been fabricated by doping 3d transition-metal (TM) atoms into nonmagnetic semiconductors and their physical properties have been extensively explored in the last two decades [19]. However, up to now the synergy of room-temperature ferromagnetism (RTFM) and high carrier mobility in one DMS, which is essential for practical spintronic applications [20,21], is still the main challenge in the field. For instance, the model material (Ga,Mn)As grown by molecular beam epitaxy shows a record-high Curie temperature (T_C) of ~200 K [2], and a hole mobility (μ_h) of only ~10 cm^2 V^{-1} s^{-1} [22]. Recently, ferromagnetic Mn-doped SiGe thin films prepared by radio frequency (r.f.) magnetron sputtering and post-growth annealing exhibit a T_C of ~280 K (~220 K), which is still lower than room temperature, and a corresponding μ_h of ~500 cm^2 V^{-1} s^{-1} (~1000 cm^2 V^{-1} s^{-1}) [12], showing a large increase in both T_C and μ_h with respect to (Ga,Mn)As. Since group-IV semiconductors are compatible with conventional integrated circuit manufacturing techniques [23] and ideal for spintronic manipulations such as ultrafast coherent control of hole spin qubit [24], it will be highly desirable to push up the T_C and μ_h values further in the SiGe-based DMSs for spintronic applications at room temperature.

In this work, single crystalline SiGe thin films are epitaxially grown on intrinsic Ge (100) substrates by ultra-high vacuum chemical vapor deposition (UHV/CVD) [25]. Then Mn element is doped into the SiGe thin films by ion-implantation at liquid-nitrogen temperature and subsequent rapid thermal annealing (RTA). The magnetization measurements show that the obtained Mn-doped SiGe thin films exhibit a T_C up to 309 K, and the X-ray magnetic circular dichroism (XMCD) characterizations confirm the spin and orbital magnetic moment contributions from the substitutional Mn element. Magneto-transport measurements at high magnetic fields reveal a record-high μ_h of ~1230 cm^2 V^{-1} s^{-1} at 300 K, owing to the tensile strain and crystalline quality of the films. Our results may excite immediate interest and spur new research in group-IV-based semiconductor spintronics and related applications.

EXPERIMENTAL SECTION

Sample preparation

Intrinsic Ge (100) wafers were ultrasonically cleaned with acetone, alcohol, and deionized water, and then dipped in dilute HCl solution. Then the wafers were exposed to ozone in one atmosphere pressure at room temperature for 30 min, in order to strongly diminish Ge substoichiometric oxides. Subsequently, the wafers were immediately loaded into the chambers of UHV/CVD with a base pressure of 5×10^{-8} Pa and then thermally annealed at 650°C for 30 min, so as to deoxidize, rendering a fresh and smooth surface. After that, a 70-nm-thick Ge buffer layer was epitaxially grown on the Ge wafers using GeH_4 precursor at a fixed flow rate of 5 sccm (standard cubic centimeter per minute) at 260°C. A 140-nm-thick $Si_{0.2}Ge_{0.8}$ film was epitaxially grown with a flow rate ratio of Si_2H_6:GeH_4 ~0.5:8. Then, the Mn ion implantation was performed at 120 keV with three

[1] College of Physics, Sichuan University, Chengdu 610064, China
[2] Key Laboratory of Radiation Physics and Technology, Ministry of Education, Institute of Nuclear Science and Technology, Sichuan University, Chengdu 610064, China
[3] College of Physics, Xiamen University, Xiamen 361005, China
* Corresponding author (email: gxiang@scu.edu.cn)

different doses (5×10^{15}, 1×10^{16}, and 1.5×10^{16} Mn^+/cm^2) at liquid-nitrogen temperature. Finally, the RTA was performed for the ion-implanted samples at 800°C for 30 s in 95% Ar/5% H_2 atmosphere by using an RTA furnace (NBD-HR1200-110IT).

Characterization

The strain and crystal quality of the samples were evaluated by high-resolution double crystal X-ray diffraction (DCXRD) (PANalytical X'pert Pro MRD, Cu Kα1 with λ = 0.154 nm), grazing incidence X-ray diffraction (GIXRD) (PANalytical Empyrean, Cu Kα with λ = 0.154 nm) and transmission electron microscopy (TEM, FEI Tecnai F30) measurements. The cross-section samples were prepared by a focus ion beam (FIB) milling procedure in a Helios (Tescan LYRA 3 XMU). The distribution and chemical states of Mn element in the SiGe matrix were evaluated by spherical aberration corrected TEM (ACTEM, FEI Titan G2 300) and X-ray photoelectron spectroscopy (XPS, Thermo Scientific Escalab250Xi) measurements. To avoid the influence of surface contaminates, a 50-nm-thick Ar ion etching was applied to the samples before the XPS measurement. The magnetic properties were measured by a superconducting quantum interference device (SQUID, Quantum Design MPMS XL-7). X-ray absorption spectroscopy (XAS) and XMCD were arisen from pairs of soft X-ray absorption spectra (μ^+/μ^-) and measured with circularly polarized X-rays with ±1 T magnetic fields applied to the samples. Hall bar-shaped devices (width 400 μm and length 1300 μm) were fabricated by standard photolithography and wet etching for transport measurements. In the transport measurements, a water-cooling magnet (WM-5 at High Magnetic Field Laboratory at Hefei, Chinese Academy of Sciences) was used. The current was applied by the Keithley 6221 instrument, and the horizontal and longitudinal voltages were measured by an SR830 Lock-In Amplifier.

RESULTS AND DISCUSSION

Structural properties

The 140-nm-thick undoped $Si_{0.2}Ge_{0.8}$ thin films were epitaxially grown on intrinsic Ge (100) substrates by UHV/CVD. The growth details can be found in our previous work [25]. For convenience, the undoped samples are named as M0. A series of Mn-doped $Si_{0.2}Ge_{0.8}$ thin films were fabricated by Mn ion implantation at liquid-nitrogen temperature and subsequent RTA. The Mn ion-implantations was performed at 120 keV with three different doses (5×10^{15}, 1×10^{16}, and 1.5×10^{16} Mn^+/cm^2), and the RTA was performed at 800°C for 30 s in 95% Ar/5% H_2 atmosphere. For convenience, the obtained samples $Si_{0.2}Ge_{0.8}$:$Mn_{0.01}$, $Si_{0.2}Ge_{0.8}$:$Mn_{0.02}$, and $Si_{0.2}Ge_{0.8}$:$Mn_{0.03}$ are named as M1, M2, and M3, respectively.

The structure of undoped M0 was first studied. Fig. 1a shows the typical cross-sectional TEM image of M0. No obvious interface between the epitaxial Ge buffer layer and the Ge substrate is observed, owing to the elaborate surface treatment of the substrate before the buffer growth [25]. The interface between the epitaxial $Si_{0.2}Ge_{0.8}$ layer and the Ge buffer layer can be clearly seen, probably because of the lattice mismatch between the two epilayers. The high-resolution TEM (HRTEM) image along with the fast Fourier-transform (FFT) and inverse FFT (IFFT) in Fig. 1c–e indicate that the high-quality single crystalline $Si_{0.2}Ge_{0.8}$ layer is epitaxially grown. The lattice constant of the $Si_{0.2}Ge_{0.8}$ layer is 5.64 Å calculated from the (111) plane spacing of 3.26 Å, bigger than that (5.61 Å) of unstrained $Si_{0.2}Ge_{0.8}$ calculated by Vegard's law [26], revealing that the $Si_{0.2}Ge_{0.8}$ layer is tensile-strained. Notably, high-resolution

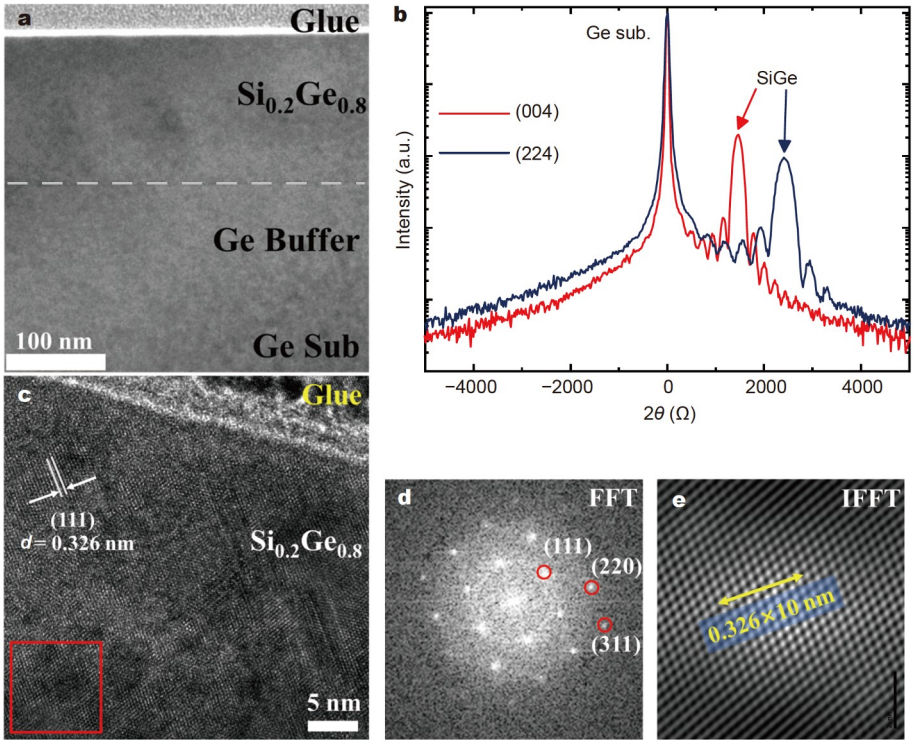

Figure 1 (a) Cross-sectional TEM and (b) high-resolution DCXRD rocking curves of (004) and (224) facets of M0. (c) HRTEM image of $Si_{0.2}Ge_{0.8}$ layer with (d) FFT and (e) IFFT images (corresponding to the red selected area in (c)) of M0.

DCXRD rocking curves of the (004) and (224) facets in Fig. 1b clearly show that the single crystalline $Si_{0.2}Ge_{0.8}$ epilayer is uniformly strained.

The microstructures of M1, M2, and M3 were then characterized. The samples show similar results, and for simplicity we take M2 as a typical example. Fig. 2a shows the HRTEM image and the corresponding FFT and IFFT images of M2. One can see that the sample becomes polycrystalline after the ion implantation and RTA, but its crystalline quality is obviously better than those of the samples prepared by r.f. magnetron sputtering and post-growth annealing [12]. No secondary phases or Mn-related clusters are shown in the HRTEM images and slightly fuzzy elements are arranged in the FFT, revealing reasonably good crystallization of the sample. The lattice constant (5.79 Å) can be acquired from the (111) plane spacing (3.34 Å), indicating a larger tensile strain in M2 than that in M0. This can be explained by the incorporation of Mn atoms with a larger atomic radius than that of Si/Ge atoms in the SiGe lattice. Fig. 2b shows the spherical ACTEM with energy dispersive spectroscopy (EDS) of M2. It shows that Mn element is distributed homogeneously in the sample, suggesting that Mn has been incorporated into the $Si_{0.2}Ge_{0.8}$ matrix. Although the Mn equilibrium solubility in the SiGe lattice is very low ($<10^{-7}$ at%) [27], a few percent Mn dopants in the SiGe lattice have been incorporated by the non-equilibrium process of low-temperature ion implantation and subsequence RTA.

Then the crystal structures and the Mn chemical states of M1, M2, and M3 were further investigated. Fig. 2c shows the GIXRD patterns of the samples. As the Mn concentration increases, the relative intensity of the (111) peaks decreases and the full width at half maximum (FWHM) increases, indicating that the crystallization becomes worse. The SiGe grain sizes of M1, M2, and M3 can be obtained from the Scherrer formula as 24, 21 and 20 nm, respectively. Notably, all the peaks shift left relative to those of unstrained $Si_{0.2}Ge_{0.8}$ sample (purple dash lines in Fig. 2c), indicating again tensile strain in all the Mn-doped samples. In addition, there is a peak with 1/6 intensity of (220) peak at 76.8° only in the pattern of M3, which may come from some unknown secondary phases caused by the most heavily implanted Mn ions in M3. Fig. 2d shows the XPS spectra of Mn 2p state in M2. M1 and M3 show similar results (not shown). The Mn $2p_{3/2}$ peak has an asymmetrical shape caused by multi-electron processes [28]. By Lorentzian-Gaussian fitting, this peak can be divided into two peaks at 639.3 and 640.5 eV, corresponding to Mn^0 and Mn^{2+} states, respectively [29–31]. No other higher atomic valences of Mn (such as Mn^{4+} $2p_{3/2}$ peak at 642.4 eV) are detected. Since a Mn atom shows a zero valance state in an interstitial site and shows a divalent state in a substitutional site in the SiGe lattice [32], the Mn atoms both exist in interstitial sites and substitutional sites in our samples owing to the ion implantation process and subsequent RTA activation process [33]. Moreover, the peak area of divalent state Mn $2p_{3/2}$ is larger than that of zero valance state, inferring that Mn atoms are mainly in substitutional sites. Consequently, substitutional Mn atoms could provide both holes and local magnetic moments in SiGe.

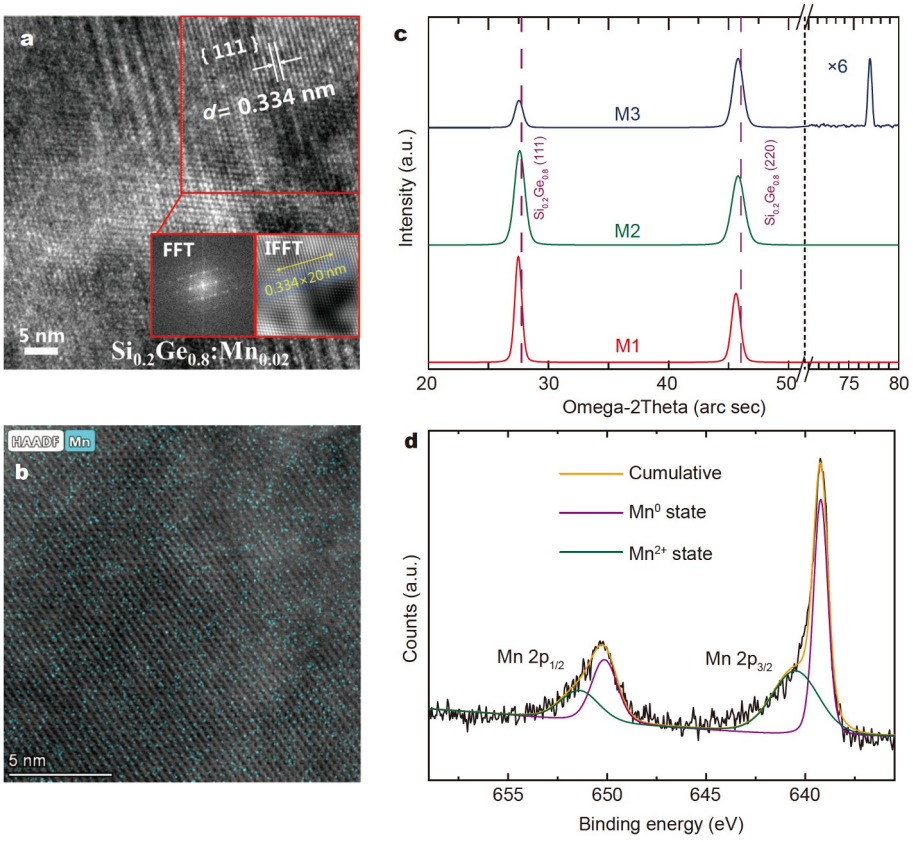

Figure 2 (a) The HRTEM image of M2. The insets show the FFT and IFFT images. (b) Cross-sectional ACTEM with Mn elementary EDS mapping of M2. (c) GIXRD patterns of M1, M2, and M3, where the purple dash lines represent the positions of unstrained $Si_{0.2}Ge_{0.8}$ (111) and (220) peaks, respectively. (d) XPS spectra results of M2.

Ferromagnetic properties

The magnetic properties of M1, M2, and M3 were measured by SQUID and shown in Fig. 3. In the measurements, the magnetic field was applied in plane. Fig. 3a shows zero-field cooled (ZFC) and 20-Oe FC magnetization of M1, M2, and M3 as the function of temperature. The convex shape of curves over the whole temperature range is a typical feature of weakly localized hole exchange interactions in ferromagnetic semiconductors [1,2,14,16]. In the low temperature range, the FC magnetization is slightly stronger than the ZFC one, which has also been observed in typical ferromagnetic semiconductors [1,7,9,12,16]. Both the FC and ZFC magnetizations sharply decrease and drop to zero near the T_C. The T_C values of M1, M2, and M3 are 294, 304, and 309 K, respectively, gradually increasing with the Mn concentration. As we know, $MnSi_{1.7}$ (Mn_4Si_7, $Mn_{11}Si_{19}$, or $Mn_{15}Si_{26}$), the energetically favorable manganese silicide phase [34,35], shows a dramatic decrease in ZFC magnetization curve below 25 K, and Ge_3Mn_5 and Ge_8Mn_{11}, the most common manganese germanide phases [17,36–39], show ferromagnetic behavior between 50 and 296 K [38,39] and between 150 and 285 K (the latter also shows antiferromagnetic ordering below 150 K) [17,37], respectively. The lack of above-mentioned magnetic features indicates that the ferromagnetism in our samples does not originate from those Mn-related secondary phases. Fig. 3b shows the magnetization *vs.* magnetic field curves of M2. The hysteresis loops are observed at different temperatures up to 300 K, and the coercive fields decrease as the temperature increases, which are clear signs of ferromagnetic ordering. M1 and M3 show similar results. The saturation magnetization is found to increase with increasing Mn concentration. Notably, the saturation magnetizations in Fig. 3b are ~4 emu cm^{-3} at 2 K and ~1.6 emu cm^{-3} at room temperature, higher than the previously-reported values (1 emu cm^{-3} at T = 5 K and 0.45 emu cm^{-3} at 293 K) in the GeMn system [40].

Moreover, to reveal the spintronic states of magnetic atoms as well as the origin of ferromagnetism in our Mn-doped SiGe thin films, XAS and XMCD measurements were performed. Fig. 3c, d show the typical results for M2. In the measurements, two XAS for parallel (μ^+) and antiparallel (μ^-) alignments of the photon helicity are recorded in a total electron yield grazing incidence mode under a magnetic field of 1 T at 300 K. As shown in Fig. 3c, two prominent XAS peaks are observed at around 640 and 650 eV, corresponding to the Mn L_3 and L_2 absorption edges resulting from the transitions from the Mn $2p_{3/2}$ and $2p_{1/2}$ core level states to the unoccupied 3d state, respectively. The multiple-peak structure is very similar to that of $Ga_{0.953}Mn_{0.047}As$ [41] and $Ge_{0.96}Mn_{0.04}$ [42], and consistent with the calculation results based on the atomic multiplet theory of Mn^{2+} ($3d^5$) [43], indicating that the electronic valence state of Mn atoms is +2 and Mn atoms are mainly in the substitutional sites hybridizing with Si or Ge 4p-states in the SiGe matrix. This is consistent with the p-type characteristics of our samples shown in Fig. 4, considering that one interstitial Mn atom with two donors can neutralize two holes provided by one substitutional Mn atom [44]. The XAS peaks of interstitial Mn are invisible because their magnitude is subordinate and their line shapes are similar to those of substitutional Mn [45]. Meanwhile, Mn oxide and precipitates of second phases such as Mn_5Ge_3 are excluded, since their different line shapes are absent in the spectra [38,46–48]. As shown in Fig. 3d, an XMCD spectrum is gathered from the difference between μ^+ and μ^- ($\Delta\mu = \mu^+ - \mu^-$). Following the XMCD sum rule [49,50], the spin and orbital magnetic moment (m_{spin} and m_{orb}) of M2 at 300 K can be obtained independently as m_{spin} = 0.021 μB atom^{-1} and m_{orb} = 0.067 μB atom^{-1}, respec-

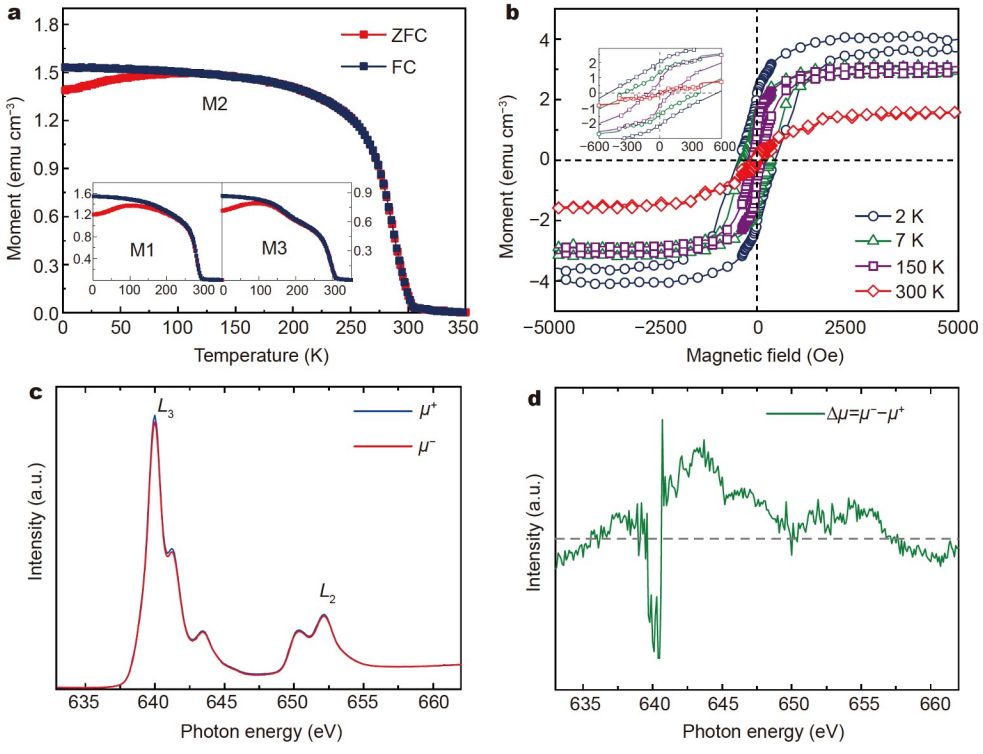

Figure 3 (a) Temperature dependence of the magnetization of M2 (M1 and M3 shown in the insets). (b) Magnetic hysteresis loops of M2. (c) XAS spectra of the parallel (μ^+) and antiparallel (μ^-) alignments of the photon helicity and (d) XMCD spectrum of M2.

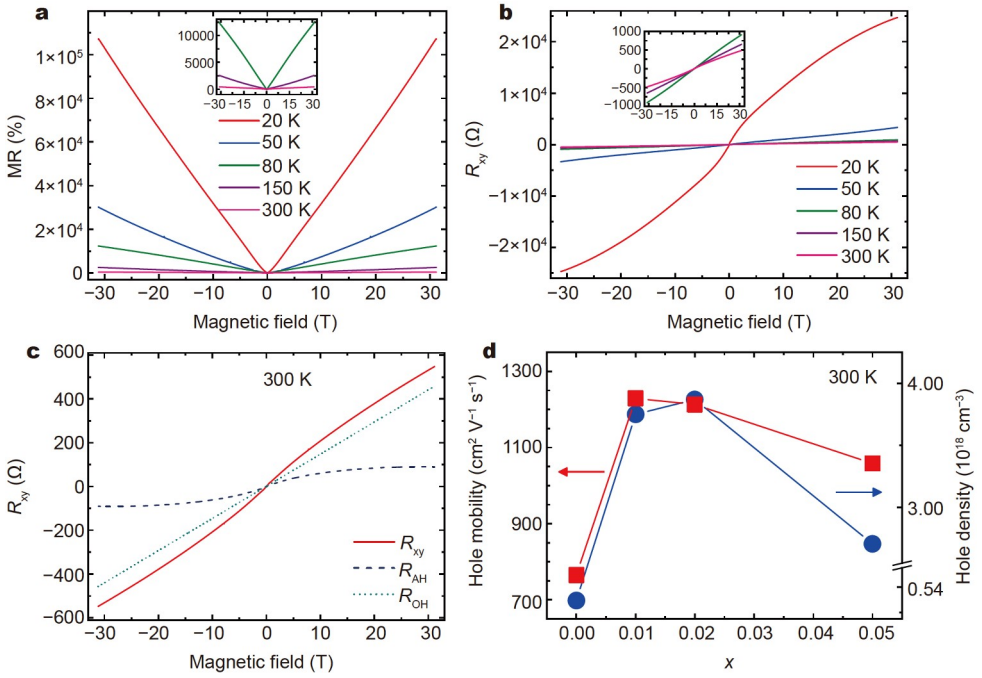

Figure 4 Magnetic field dependences of (a) MR and (b) R_{xy} of M2 at different temperatures. Insets show the curves at higher temperatures. (c) The decomposition of R_{xy} into ordinary R_{OH} and anomalous R_{AH} at 300 K. (d) The μ_h and hole density *vs.* the Mn doping concentration (x) at 300 K.

tively. In short, all the measurements indicate that the ferromagnetism in our samples should be contributed by Mn dopants dispersed at the substitutional sites in the SiGe matrix, which provide both the holes and local magnetic moments. The ferromagnetism comes up when the itinerant holes align the local magnetic moments of the Mn atoms in one direction through the exchange coupling [12,17,20], and gets enhanced by the tensile strain in the samples [51].

Transport properties

In order to estimate the carrier mobility (μ) and concentration in our magnetic semiconducting samples, their magneto-transport properties under a high magnetic field up to 31 T were studied. The carrier mobility and concentration in a DMS are notoriously difficult to estimate because of the co-existence of anomalous Hall effect (AHE) and ordinary Hall effect (OHE) in the sample. The Hall resistance (R_{xy}) in a magnetic sample is defined as $R_{xy} = R_0B/d + R_SM/d$ [52], where R_0 represents ordinary Hall coefficient, R_S represents anomalous Hall coefficient and is a function of longitudinal resistivity ρ_{xx} [22,52], d is the thickness, B is the external applied magnetic field, and M is the magnetization of the sample. Notably, the OHE term (R_0B/d) increases with B, and gets large when B is high. Meanwhile, the AHE term (R_SM/d) is dependent on M and R_S, where M has a small value and R_S has a finite value at a high temperature close to the T_C, as shown in Fig. 3a and Fig. 4a. Therefore, with a high magnetic field of 31 T applied at 300 K, the AHE term is very small compared with the OHE term in our DMS samples. In this way, the influence of AHE can be minimized and relatively accurate carrier mobility and concentration can be obtained.

The magnetic field dependence of magnetoresistance (MR) of M2 is shown in Fig. 4a. A giant and positive MR up to ~10700% at 20 K and ~420% at 300 K are observed. The similar large positive MR has been reported in Mn-doped Ge and SiGe, which is attributed to the mechanism as follows [16,53]. At low magnetic fields, the electrical current is parallel to the local electric field and flows through the crystalline components with low resistivity. At high magnetic fields, the electrical current is deviated by the Lorentz force and flows into noncrystalline components with high resistivity. As a result, a large positive MR is observed. The temperature-dependent resistivity at zero field shows a typical characteristic of a doped semiconductor, which increases exponentially at low temperatures and saturates and finally decreases at high temperatures, similar to the previous result [12].

The magnetic field dependence of R_{xy} of M2 is shown in Fig. 4b. Clear AHE signals are observed, indicating the ferromagnetic ordering in the sample. The positive slope of R_{xy} shows that the majority carriers are holes. As shown in Fig. 4c, the Hall resistance at 300 K can be decomposed into ordinary Hall resistance (R_{OH}) and anomalous Hall resistance (R_{AH}), where R_{OH} is obtained from the invariant slope at the high magnetic field region (20T-31T) and R_{AH} is obtained by subtracting R_{xy} by R_{OH}. Obviously, R_{AH} is much smaller than R_{OH}, as we have discussed above. In this way, the μ_h and hole density can be obtained from the R_{OH} at 300 K. Fig. 4d shows the carrier density and mobility results of M0, M1, M2, and M3 at 300 K. The majority carriers in the undoped SiGe sample (M0) are holes, owing to the existence of inevitable vacancy defects in the lattice [25,54,55]. Since substitutional Mn dopants provide additional holes, the hole density in M1 and M2 increases about one order compared with that in M0. The hole density in M3 is smaller than that in M2, because Mn-related secondary phase precipitations start to come up, as shown in Fig. 2c. There is a significant increase of μ_h in M1 with respect to M0, because of the enhanced tensile strain in the $Si_{0.2}Ge_{0.8}$ matrix due to the Mn dopants [12,56,57]. In the doped samples, the μ_h monotonically decreases with the doping density, which can be explained by

impurity scattering [58]. The hole density increases with the temperature owing to the impurity ionization. Besides the ionized impurity scattering ($\mu \sim T^{1.5}$) [12] and lattice vibration scattering, the increase of tensile strain with the temperature due to the larger thermal expansion coefficient of Ge than that of SiGe also exists in the samples, which results in the enhancement of hole mobility. Notably, the hole mobility in our samples reaches up to ~1230 $cm^2 V^{-1} s^{-1}$ at room temperature, which is record-high in all the previously-reported DMSs and 120 times that of (Ga,Mn)As measured at a high magnetic field [22]. The higher hole mobility is probably caused by the tensile strain-induced separation of light hole and heavy hole at the top of valence band in SiGe [56] and reasonably good crystalline quality in the samples.

CONCLUSIONS

In this work, we have fabricated Mn-doped SiGe thin films by UHV/CVD and liquid-nitrogen temperature Mn ion-implantation aided with RTA. The crystalline quality of samples is much better than that of the samples prepared by r.f. magnetron sputtering and post-growth annealing [12]. The samples exhibit hole-mediated ferromagnetism up to 309 K, where the local magnetic moments and hole carriers are provided by the substitutional Mn dopants. By measuring the transport properties with a magnetic field up to 31 T at 300 K to minimize the influence of AHE, the μ_h of the samples is obtained, which reaches a record-high value of ~1230 $cm^2 V^{-1} s^{-1}$, owing to the crystalline quality and tensile strain-induced band modulation of the samples. The Mn-doped SiGe thin films with RTFM and high carrier mobility may be useful for further basic research and potential applications of group-IV-based semiconductor spintronics.

Received 26 January 2022; accepted 7 March 2022; published online 14 April 2022

1 Ohno H, Shen A, Matsukura F, *et al.* (Ga,Mn)As: A new diluted magnetic semiconductor based on GaAs. Appl Phys Lett, 1996, 69: 363–365
2 Chen L, Yang X, Yang F, *et al.* Enhancing the Curie temperature of ferromagnetic semiconductor (Ga,Mn)As to 200 K *via* nanostructure engineering. Nano Lett, 2011, 11: 2584–2589
3 Jungwirth T, Wang KY, Mašek J, *et al.* Prospects for high temperature ferromagnetism in (Ga,Mn)As semiconductors. Phys Rev B, 2005, 72: 165204
4 Cui JB, Gibson UJ. Electrodeposition and room temperature ferromagnetic anisotropy of Co and Ni-doped ZnO nanowire arrays. Appl Phys Lett, 2005, 87: 133108
5 Fan JP, Li XL, Quan ZY, *et al.* Tunable magnetic and transport properties of p-type ZnMnO films with n-type Ga, Cr, and Fe codopants. Appl Phys Lett, 2013, 102: 102407
6 Brieler FJ, Grundmann P, Fröba M, *et al.* Formation of $Zn_{1-x}Mn_xS$ nanowires within mesoporous silica of different pore sizes. J Am Chem Soc, 2004, 126: 797–807
7 Zhao GQ, Lin CJ, Deng Z, *et al.* Single crystal growth and spin polarization measurements of diluted magnetic semiconductor (BaK)-$(ZnMn)_2As_2$. Sci Rep, 2017, 7: 14473
8 Gu G, Zhao G, Lin C, *et al.* Asperomagnetic order in diluted magnetic semiconductor $(Ba,Na)(Zn,Mn)_2As_2$. Appl Phys Lett, 2018, 112: 032402
9 Zhao K, Deng Z, Wang XC, *et al.* New diluted ferromagnetic semiconductor with Curie temperature up to 180 K and isostructural to the '122' iron-based superconductors. Nat Commun, 2013, 4: 1442
10 Bolduc M, Awo-Affouda C, Stollenwerk A, *et al.* Above room temperature ferromagnetism in Mn-ion implanted Si. Phys Rev B, 2005, 71: 33302
11 Collins BA, Chu YS, He L, *et al.* Dopant stability and strain states in Co and Mn-doped Ge (001) epitaxial films. Phys Rev B, 2008, 77: 193301
12 Wang H, Sun S, Lu J, *et al.* High Curie temperature ferromagnetism and high hole mobility in tensile strained Mn-doped SiGe thin films. Adv Funct Mater, 2020, 30: 2002513
13 Kazakova O, Kulkarni JS, Holmes JD, *et al.* Room-temperature ferromagnetism in $Ge_{1-x}Mn_x$ nanowires. Phys Rev B, 2005, 72: 094415
14 Xiu F, Wang Y, Kim J, *et al.* Electric-field-controlled ferromagnetism in high-Curie-temperature $Mn_{0.05}Ge_{0.95}$ quantum dots. Nat Mater, 2010, 9: 337–344
15 Qiao S, Hou D, Tang G. The structure and magnetic properties in heavily Mn-doped Mn_xSi_{1-x} films. Solid State Commun, 2015, 203: 21–25
16 Jamet M, Barski A, Devillers T, *et al.* High-Curie-temperature ferromagnetism in self-organized $Ge_{1-x}Mn_x$ nanocolumns. Nat Mater, 2006, 5: 653–659
17 Park YD, Hanbicki AT, Erwin SC, *et al.* A Group-IV ferromagnetic semiconductor: Mn_xGe_{1-x}. Science, 2002, 295: 651–654
18 Gambardella P, Claude L, Rusponi S, *et al.* Surface characterization of Mn_xGe_{1-x} and $Cr_yMn_xGe_{1-x-y}$ dilute magnetic semiconductors. Phys Rev B, 2007, 75: 125211
19 Dietl T, Sato K, Fukushima T, *et al.* Spinodal nanodecomposition in semiconductors doped with transition metals. Rev Mod Phys, 2015, 87: 1311–1377
20 Dietl T, Ohno H. Dilute ferromagnetic semiconductors: Physics and spintronic structures. Rev Mod Phys, 2014, 86: 187–251
21 Park S , Kim P , Lee YP, *et al.* Realization of room-temperature ferromagnetism and of improved carrier mobility in Mn-doped ZnO film by oxygen deficiency, introduced by hydrogen and heat treatments. Adv Mater, 2007, 19: 3496–3500
22 Matsukura F, Ohno H, Shen A, *et al.* Transport properties and origin of ferromagnetism in (Ga,Mn)As. Phys Rev B, 1998, 57: R2037–R2040
23 Sverdlov V, Selberherr S. Silicon spintronics: Progress and challenges. Phys Rep, 2015, 585: 1–40
24 Wang K, Xu G, Gao F, *et al.* Ultrafast coherent control of a hole spin qubit in a germanium quantum dot. Nat Commun, 2022, 13: 206
25 Wang J, Shen L, Lin G, *et al.* Homoepitaxy of Ge on ozone-treated Ge (100) substrate by ultra-high vacuum chemical vapor deposition. J Cryst Growth, 2019, 507: 113–117
26 Denton AR, Ashcroft NW. Vegard's "law". Phys Rev A, 1991, 43: 3161–3164
27 Woodbury HH, Tyler WW. Properties of germanium doped with manganese. Phys Rev, 1955, 100: 659–662
28 Bulavchenko OA, Vinokurov ZS, Afonasenko TN, *et al.* Reduction of mixed Mn-Zr oxides: *In situ* XPS and XRD studies. Dalton Trans, 2015, 44: 15499–15507
29 Myers CE, Franzen HF, Anderegg JW. X-ray photoelectron spectra and bonding in transition-metal phosphides. Inorg Chem, 1985, 24: 1822–1824
30 Kim SK, Cho YC, Jeong SY, *et al.* High-temperature ferromagnetism in amorphous semiconductor Ge_3Mn thin films. Appl Phys Lett, 2007, 90: 192505
31 Qiao S, Hou D, Wei Y, *et al.* Ferromagnetism in Mn_xGe_{1-x} films prepared by magnetron sputtering. J Magn Magn Mater, 2009, 321: 2446–2450
32 Zhou S, Schmidt H. Mn-doped Ge and Si: A review of the experimental status. Materials, 2010, 3: 5054–5082
33 Li AP, Zeng C, van Benthem K, *et al.* Dopant segregation and giant magnetoresistance in manganese-doped germanium. Phys Rev B, 2007, 75: 201201
34 Zhou S, Potzger K, Zhang G, *et al.* Structural and magnetic properties of Mn-implanted Si. Phys Rev B, 2007, 75: 085203
35 Awo-Affouda C, Bolduc M, Huang MB, *et al.* Observation of crystallite formation in ferromagnetic Mn-implanted Si. J Vacuum Sci Tech A-Vacuum Surfs Films, 2006, 24: 1644–1647
36 Wang H, Sun S, Xu J, *et al.* Microstructure and ferromagnetism of heavily Mn doped SiGe thin flims. Chin Phys B, 2020, 29: 057504
37 Wang Y, Zou J, Zhao Z, *et al.* Direct structural evidences of $Mn_{11}Ge_8$ and Mn_5Ge_2 clusters in $Ge_{0.96}Mn_{0.04}$ thin films. Appl Phys Lett, 2008, 92:

101913
38 Biegger E, Stäheli L, Fonin M, *et al.* Intrinsic ferromagnetism *versus* phase segregation in Mn-doped Ge. J Appl Phys, 2007, 101: 103912
39 Passacantando M, Ottaviano L, D'Orazio F, *et al.* Growth of ferromagnetic nanoparticles in a diluted magnetic semiconductor obtained by Mn^+ implantation on Ge single crystals. Phys Rev B, 2006, 73: 195207
40 Ottaviano L, Continenza A, Profeta G, *et al.* Room-temperature ferromagnetism in Mn-implanted amorphous Ge. Phys Rev B, 2011, 83: 134426
41 Ishiwata Y, Watanabe M, Eguchi R, *et al.* Manganese concentration and low-temperature annealing dependence of $Ga_{1-x}Mn_xAs$ by X-ray absorption spectroscopy. Phys Rev B, 2002, 65: 233201
42 Ottaviano L, Passacantando M, Verna A, *et al.* Mn $L_{2,3}$ X-ray absorption spectra of a diluted Mn-Ge alloy. Appl Phys Lett, 2007, 90: 242105
43 van der Laan G, Kirkman IW. The 2p absorption spectra of 3d transition metal compounds in tetrahedral and octahedral symmetry. J Phys-Condens Matter, 1992, 4: 4189–4204
44 Edmonds KW, Farley NRS, Campion RP, *et al.* Surface effects in Mn $L_{3,2}$ X-ray absorption spectra from (Ga,Mn)As. Appl Phys Lett, 2004, 84: 4065–4067
45 Picozzi S, Ottaviano L, Passacantando M, *et al.* X-ray absorption spectroscopy in Mn_xGe_{1-x} diluted magnetic semiconductor: Experiment and theory. Appl Phys Lett, 2005, 86: 062501
46 Hirai C, Sato H, Kimura A, *et al.* Mn 2p-3d soft X-ray magnetic circular dichroism study of Mn_5Ge_3. Physica B-Condensed Matter, 2004, 351: 341–343
47 Sangaletti L, Magnano E, Bondino F, *et al.* Interface formation and growth of ferromagnetic thin layers in the Mn:Ge(111) system probed by dichroic soft X-ray spectroscopies. Phys Rev B, 2007, 75: 153311
48 de Padova P, Ayoub JP, Berbezier I, *et al.* $Mn_{0.06}Ge_{0.94}$ diluted magnetic semiconductor epitaxially grown on Ge(001): Influence of Mn_5Ge_3 nanoscopic clusters on the electronic and magnetic properties. Phys Rev B, 2008, 77: 045203
49 Thole BT, Carra P, Sette F, *et al.* X-ray circular dichroism as a probe of orbital magnetization. Phys Rev Lett, 1992, 68: 1943–1946
50 Carra P, Thole BT, Altarelli M, *et al.* X-ray circular dichroism and local magnetic fields. Phys Rev Lett, 1993, 70: 694–697
51 Weng H, Dong J. First-principles investigation of transition-metal-doped group-IV semiconductors: R_xY_{1-x} (R = Cr, Mn, Fe; Y = Si, Ge). Phys Rev B, 2005, 71: 035201
52 Nagaosa N, Sinova J, Onoda S, *et al.* Anomalous Hall effect. Rev Mod Phys, 2010, 82: 1539–1592
53 Nie T, Tang J, Kou X, *et al.* Enhancing electric-field control of ferromagnetism through nanoscale engineering of high-T_c Mn_xGe_{1-x} nanomesh. Nat Commun, 2016, 7: 12866
54 Mchedlidze T, Yonenaga I. Hall effect measurements on Si_xGe_{1-x} bulk alloys. MRS Proc, 1997, 442: 381–384
55 Shen L, Zhang X, Lu J, *et al.* The effect of vacancy defects on the conductive properties of SiGe. Phys Lett A, 2021, 386: 126993
56 Fischetti MV, Laux SE. Band structure, deformation potentials, and carrier mobility in strained Si, Ge, and SiGe alloys. J Appl Phys, 1996, 80: 2234–2252
57 Chu M, Sun Y, Aghoram U, *et al.* Strain: A solution for higher carrier mobility in nanoscale MOSFETs. Annu Rev Mater Res, 2009, 39: 203–229
58 Prince MB. Drift mobilities in semiconductors. I. Germanium. Phys Rev, 1953, 92: 681–687

Acknowledgements This work was supported by the National Key Research and Development Program of China (2017YFB0405702) and the National Natural Science Foundation of China (52172272). The authors thank the High Magnetic Field Laboratory of Chinese Academy of Sciences for the help in the high magnetic field transport measurements of the samples, and the Analytical & Testing Center of Sichuan University for the TEM measurements.

Author contributions Shen L prepared the samples and performed the experiments; Zhang X and Li C provided the resources and supervised the project; Wang JQ and Wang JY prepared the samples; Shen L, Zhang X, and Xiang G wrote the paper; Xiang G designed and supervised the project. All authors contributed to the general discussion.

Conflict of interest The authors declare that they have no conflict of interest.

Limeng Shen is a PhD student at Sichuan University under the supervision of Prof. Gang Xiang. His current research interests focus on the diluted magnetic semiconductors based on group-IV as well as the related functional devices.

Gang Xiang earned his PhD degree in condensed matter physics from Pennsylvania State University-University Park in 2006. Then he worked at Pennsylvania State University-University Park (2006–2007) and also at Ohio State University-Columbus (2007–2010) as a postdoctoral researcher. He joined Sichuan University in 2010. His research interests include the design and fabrication of magnetic materials including diluted magnetic semiconductors and transition metal chalcogenides, and their spintronic and electronic applications.

具有室温铁磁性和高空穴迁移率的锰掺杂硅锗薄膜

申笠蒙[1,2], 张析[1,2], 王佳琪[3], 汪建元[3], 李成[3], 向钢[1,2*]

摘要 本文采用超高真空化学气相沉积系统在锗衬底上外延生长了第IV族硅锗薄膜, 然后通过离子注入和快速热退火进行锰元素掺杂. 结构测试表明, 外延的硅锗薄膜是具有均匀拉伸应变的单晶, 随后的离子注入和快速热退火使其变为多晶. 磁性测试表明, 退火后的薄膜表现出依赖于锰掺杂浓度的铁磁性, 居里温度最高可达309 K; X射线磁圆二色谱揭示了替代位锰元素的自旋和轨道磁矩. 为最大限度地减少反常霍尔效应的影响, 磁输运测试在高达31 T的强磁场下进行, 该薄膜在300 K温度下空穴迁移率达到创纪录的~1230 $cm^2 V^{-1} s^{-1}$. 此高迁移率归因于样品较高的结晶质量和拉伸应变对能带的调制. 本文首次展示了具有室温铁磁性和高载流子迁移率的锰掺杂硅锗薄膜, 有望促进基于第IV族半导体的自旋电子材料与器件的实际应用.

